

RESEARCH ARTICLE | FEBRUARY 09 2023

Divergence-free turbulent inflow data from realistic covariance tensor

Yann Dreze  ; Muting Hao (郝苜婷) ; Luca di Mare



Physics of Fluids 35, 025120 (2023)

<https://doi.org/10.1063/5.0136568>



Export
Citation

CrossMark

Articles You May Be Interested In

Generation of turbulent inflow data from realistic approximations of the covariance tensor

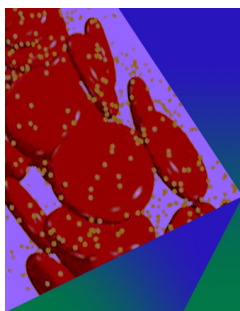
Physics of Fluids (November 2022)

Anisotropy of the Reynolds stress tensor in the wakes of wind turbine arrays in Cartesian arrangements with counter-rotating rotors

Physics of Fluids (January 2015)

Direct numerical simulation of hypersonic wall-bounded turbulent flows: An improved inflow boundary condition and applications

Physics of Fluids (March 2023)



Physics of Fluids

Special Topic: Flow and Forensics

Submit Today!



Divergence-free turbulent inflow data from realistic covariance tensor

Cite as: Phys. Fluids **35**, 025120 (2023); doi: [10.1063/5.0136568](https://doi.org/10.1063/5.0136568)

Submitted: 27 November 2022 · Accepted: 24 January 2023 ·

Published Online: 9 February 2023






View Online



Export Citation



CrossMark

Yann Dreze,^{a)}  Muting Hao (郝苜婷),  and Luca di Mare 

AFFILIATIONS

Department of Engineering Science, Oxford Thermofluids Institute, University of Oxford, Oxford OX2 0ES, United Kingdom

^{a)} Author to whom correspondence should be addressed: yann.dreze@wadham.ox.ac.uk

ABSTRACT

Scale-resolving computational fluid dynamics (CFD) methods require carefully constructed boundary conditions to produce accurate results. The inflow data should be unsteady and the successive realizations must follow specific statistics while ideally having a particular correlation in both space and time. A method for generating synthetic correlated stochastic data from uncorrelated sequences is detailed and applied to the problem of inflow turbulence generation for CFD simulations. The technique constructs divergence-free anisotropic random fields with the sensible spectrum and complete complex correlation in space and time. A realistic two-point correlation tensor is inferred from first and second moments and a set of heuristic recommendations based on turbulent flow observations. These statistics are readily available in most practical cases making the technique highly versatile. The approach is computationally efficient with the use of eigendecomposition to reduce the resources required depending on the accuracy needed. Demonstration of the method is provided with the simulation of a turbulent channel flow and a square duct flow, and validation is done against existing numerical data.

© 2023 Author(s). All article content, except where otherwise noted, is licensed under a Creative Commons Attribution (CC BY) license (<http://creativecommons.org/licenses/by/4.0/>). <https://doi.org/10.1063/5.0136568>

I. LITERATURE SURVEY

Over the years, the development of computer capabilities has increased the popularity of large-eddy simulations (LES) and direct numerical simulations (DNS). For such scale-resolving techniques, while the precision is dictated by the computational resources available, the accuracy of the result is strongly influenced by the boundary conditions imposed, especially at the inlet. The inflow realizations must be unsteady, but it is not sufficient to superimpose uncorrelated and spectrally uniform randomness on top of a mean flow field. Because turbulent flow fields are highly correlated at small separations and have a wide range of length scales, the fluctuations generated as such will get damped out, not developing into turbulence and leading to inaccurate results. For instance, Lund *et al.* (1998) showed that specifying random uncorrelated fluctuations at the inflow of a spatially developing boundary layer leads to large underpredictions of the boundary layer characteristics downstream. The same conclusion was drawn by Le *et al.* (1997) in the simulation of a backward-facing step, highlighting the strong influence of the inflow on the result; hence, the boundary realizations should follow the specific turbulent properties of the problem studied.

Various approaches are available to generate inlet turbulence. The present section provides a brief overview of the main techniques,

for a more comprehensive analysis refer to Dhamankar *et al.* (2018) or Wu (2017). Traditionally, inflow methods can be divided into two main categories: synthetically generated turbulence under which the proposed method falls, and deterministic techniques such as turbulence-inducing simulations and inflows using precursor or co-simulating simulations. Turbulence-inducing techniques simulate the turbulent transition upstream of the domain of interest, hence not requiring the generation of correlated random data, see, for example, Rai and Moin (1993). Alternatively, a second simulation can be run *a priori* or concurrently to generate turbulent data for the main simulation. These approaches are relatively straightforward to implement, and the generated fields at the inflow are realistic but rely on an extended numerical domain of some sort and consequently bring a considerable additional computational and memory cost. Synthetic methods alleviate this issue by constructing turbulence-like fluctuations from uncorrelated data and known target properties. Preferably, synthetic generators should rely only on turbulence statistics that are readily available or inexpensive to compute. The boundary plane is placed a short distance upstream of the simulation model to allow for the synthetic turbulence to settle. The fields generally match first-order statistics immediately, but the correct covariance is usually reached only after a short distance from the boundary. The synthetic

field morphs into a physical turbulent flow, satisfying the Navier–Stokes equations. This development distance is a good indicator on the performance of a method and the validity of the assumptions made.

In recent years, novel hybrid approaches have emerged. [Spille-Kohoff and Kaltenbach \(2001\)](#), [Meux *et al.* \(2015\)](#), and [Ketterl and Klein \(2018\)](#) proposed a method based on a linear forcing term and a precursor simulation. The forcing term is used to control the fluctuations in order to achieve the desired turbulence characteristics while still being realistic as the Navier–Stokes equations are solved. Another approach studied is the application of machine learning to synthetic turbulence. In recent years, machine learning techniques have been used to better understand and predict turbulence. For inflow generation, machine learning algorithms can be trained on data collected from simulations or high-definition experiments, and can then be used to generate synthetic fluctuations that closely resemble the physical phenomenon. [Fukami *et al.* \(2019\)](#) used DNS data of a turbulent channel flow to produce inflow fields for the same case properties. A similar approach was followed by [Kim and Lee \(2020\)](#), and they successfully generated inflow boundaries at different Reynolds numbers. More recently, [Yousif *et al.* \(2022\)](#) used deep learning to generate instantaneous velocity fields for a developing boundary layer. Although machine learning models are able to accurately match turbulence statistics for various flow regimes over an extended period, their reliance on high-order statistics for training limits their current practical applications.

Synthetic methods continue to be widely used among the available options due to their versatility and relatively low computational cost. Apart from attempts based on uniformly distributed series, the earliest proposed approaches relied on a Fourier decomposition of turbulence following the well-known Kolmogorov spectra, as done by [Kondo *et al.* \(1997\)](#), who successfully simulated decaying isotropic turbulence. A second type of decomposition frequently used is orthogonal decomposition, which transform a flow field into an orthogonal basis sorted based on energy and can be applied to nonperiodic signals. The eigenfunctions represent coherent patterns present in the function of interest. The energy of each mode is scaled by its eigenvalue, offering a direct way to reduce the data needed while keeping the main features of the correlation. The estimation of how many terms in the series are necessary for an accurate representation is dependent on the length scales resolvable by the mesh and the computational method used. Eigendecomposition is useful for studying turbulent flows; [Bakewell and Lumley \(1967\)](#) applied it to extract the main structures present in the viscous sublayer of a turbulent pipe flow. [Moin and Moser \(1989\)](#) and [Nawab and di Mare \(2018\)](#) decomposed a DNS simulation of a turbulent channel using POD to understand the different eddy structures present.

A related technique was proposed by [Klein *et al.* \(2003\)](#) and followed by [di Mare *et al.* \(2006\)](#), and it employs digital filters to generate inflow data. Random uncorrelated data are filtered with a set of coefficients to obtain the prescribed one-point first- and second-order statistics as well as two-point correlation function. In most cases, the filters have a Gaussian shape to simplify the relations between the filter coefficients and the velocity correlation. Advantages of filtering digitally random data are the ability to generate prescribed statistics while keeping the signal non-periodic unlike Fourier-based inflows. Later, [Hao *et al.* \(2022\)](#) extended the method by combining the use of a digital filter and eigendecomposition. The correlation tensor is decomposed

into modes that capture the variations of the flow quantities on the inflow plane while preserving a prescribed correlation. Finally, a digital filter was created for each mode to enforce a two-time correlation. The procedure was applied to a developing boundary layer and a turbulent channel flow, and it was found to require significantly shorter development lengths compared to previous synthetic generation techniques. Efforts are also ongoing to further improve the computational performance and broaden the scope of applications for digital filtering techniques. [Treleaven *et al.* \(2020\)](#) applied a proper orthogonal decomposition to the generated filter to compress the data needed to reconstruct the filter, making the method up to eight times faster. Moreover, [Dhamankar *et al.* \(2018\)](#) has adapted the original filtering method to curvilinear grids instead of uniform grids only, extending the scope of the technique. The present method builds up on the work of [Hao *et al.* \(2022\)](#), seeking more realistic fluctuations while maintaining a computational cost similar to the original filtering technique. To achieve this, the extension utilizes a complete complex correlation function rather than a diagonal tensor and ensures the divergence-free condition is met by the filters. Additionally, the method removes the need for an approximate exponential expression of the filter by considering the spectrum of the fluctuations. Overall, significant performance improvements in terms of development length are achieved.

II. METHOD

This section describes the procedure used to generate correlated data from uncorrelated sequences based on the decomposition of the covariance tensor. In addition, a discussion about the structure of the two-point correlation tensor in turbulent wall-bounded flows is made based on observations. From there, recommendations are drawn and an approximation technique based on first-order statistics and the divergence-free condition is detailed.

A. Prescribed covariance

Correlated data a_i can be generated synthetically from an uncorrelated random set ϕ_i and some appropriately chosen coefficients. As explained by [di Mare and Jones \(2005\)](#), any symmetric factorization s_{ih} of a covariance tensor r_{ij} is an appropriate choice of coefficients. Given a random uncorrelated sequence ϕ_i , with covariance tensor δ_{ij} , the stochastic correlated data can be generated by the following equation:

$$\begin{aligned}\langle a_i a_j^* \rangle &= \langle s_{ih} \phi_h s_{jk}^* \phi_k^* \rangle = \langle \phi_h \phi_k^* \rangle s_{ih} s_{jk}^*, \\ &= \delta_{hk} s_{ih} s_{jk}^*, \\ &= s_{ih} s_{jh}^*, \\ &= r_{ij}.\end{aligned}\quad (1)$$

Using Einstein's convention, $*$ indicates the complex conjugate. To avoid periodicity in the generated data due to the finite size of the correlation tensor support, [Klein *et al.* \(2003\)](#) preferred the use of a convolution instead of multiplying the data coefficients

$$a_i = \sum_{h=-N}^N s_{ih} \phi_{i+h}. \quad (2)$$

This filter technique is capable of generating three-dimensional correlated data that can be used as inflow data if the Taylor hypothesis is

made. It has been applied successfully by Klein *et al.* (2003) and Hoepffner *et al.* (2011) to generate inflow conditions for impinging jet flows and free shear layers. However, the filter coefficients were obtained based on assumed exponential expressions; the present work alleviates these by constructing a realistic correlation tensor based on spectral and variance data.

The statistical method to reproduce correlated data relies on the ability to factorize the correlation tensor of the targeted signal in every dimension of the problem studied. An efficient way to obtain a symmetric factorization of a tensor is using an orthogonal decomposition. As explained in Sec. I, eigenanalysis linearly decomposes the turbulent flow into modes representing the coherent structure present in the data. The special case of a homogeneous direction must be treated carefully. In such an instance, the correlation tensor is circulant and eigenanalysis leads to trigonometric eigenvectors, shortening the information needed in the periodic direction to only an energy distribution. Nevertheless, as elaborated in Lumley (1981), trigonometric functions differ fundamentally from typical eigenfunctions as their spatial extent is not limited. Another difference in that case is that the modes do not represent specific structures present in the flow, rather the spectral distribution of the flow. It must be noted that other decompositions are available and can preserve the features of shape and spatial extent, see Lumley (1981).

B. Construction of the covariance tensor

A turbulent flow can be statistically described by its two-point one-time velocity correlation tensor $R_{ij}(\mathbf{x}^{(1)}, \mathbf{x}^{(2)}) = \langle u_i(\mathbf{x}^{(1)}) u_j^*(\mathbf{x}^{(2)}) \rangle$, with the symmetry property $R_{ij}(\mathbf{x}^{(1)}, \mathbf{x}^{(2)}) = R_{ji}^*(\mathbf{x}^{(2)}, \mathbf{x}^{(1)})$.

In most practical cases, the complete covariance tensor is not directly available. A reasonable estimation can be obtained based on first and second moments, directly available from an inexpensive steady RANS simulation. Klein *et al.* (2003) and Hao *et al.* (2022) proposed an expression dependent on an exponential decay function of the separation and an appropriate length scale.

$$R_{ij}(\mathbf{x}^{(1)}, \mathbf{x}^{(2)}) = (-1)^{\delta_{ij}} \sqrt{\langle u_i u_j \rangle(\mathbf{x}^{(1)}) \langle u_i u_j \rangle(\mathbf{x}^{(2)})} \times \exp \left(- \frac{\|(\mathbf{x}^{(1)} - \mathbf{x}^{(2)})\|^2}{L(\mathbf{x}^{(1)}) \cdot L(\mathbf{x}^{(2)})} \right). \quad (3)$$

The continuity equation constrains the correlation tensor as

$$\frac{\partial}{\partial x_j^{(2)}} R_{ij}(\mathbf{x}^{(1)}, \mathbf{x}^{(2)}) = 0. \quad (4)$$

In the case of a homogeneous inflow direction, which is the case for most simulations as the inflow turbulent properties are likely to be constant or at least periodic, the flow can be decomposed in Fourier series. The correlations between the complex series coefficients have been studied for a turbulent channel and a square duct. Multiple observations have been made:

- The envelope of the correlation decays as an exponential or a Gaussian shape. In some cases, the decay reaches negative values, which are necessary for the divergence-free condition to be respected. A Gaussian modulated with a cosine is well suited to approximate the behavior of the correlation.
- The imaginary part of the normal components must be anti-symmetric as per the definition of the correlation.

- The exponential decay constant is proportional to the position in the non-periodic directions and the wavelength of the mode.
- The symmetries of the correlation are dictated by the non-periodic direction—the correlation follows the symmetries present in the velocity variances.

The complete correlation tensor is Hermitian thanks to the symmetry properties, which ensures real eigenvalues. For the purpose of factorization, only the positive eigenvalues are kept as the others are non-realizable—these arise when the correlation prescribed spreads too far in space.

III. RESULTS

In this section, the method described above is applied to two test cases and the results are compared with DNS data. Particular attention is given to the settlement length needed for the synthetic fluctuations to transform into physical turbulence.

The flow equations are solved using the code H4X (Hao *et al.*, 2022; Hope-Collins and di Mare, 2023). The code is a cell-centered finite volume code based on a multiblock grid arrangement. The flow field is represented by the viscous variables: velocities, temperature, and pressure. The equations of motion for a compressible fluid are solved in conservative form. The spatial discretization is third-order accurate in space for the inviscid fluxes. Third-order accuracy is achieved on a compact stencil by using variable extrapolation. No limiter is applied. The extrapolation is based on weighted least-square gradients. The gradient stencil contains all the face neighbors of each cell. For the purpose of variable extrapolation onto a cell interface, the gradient stencil is biased by removing the contributions from the neighbor on the other side of the interface. The numerical fluxes are adapted to low Mach numbers (Hope-Collins and di Mare, 2023), and a modified pressure flux is employed. The viscous fluxes are evaluated using a second-order discretization. Advancement in time is performed using a formally second-order accurate implicit scheme. The implicit iterations are based on a dual-time stepping formulation. The code is parallelized by partitioning the blocks of the multiblock grid among the available MPI ranks. Within each rank, block operations are parallelized using OpenMP. Computations and communications are overlaid to hide the latency of the network fabric.

A. Channel flow case

The first test case is a fully developed turbulent channel flow, rendered in Fig. 1. With turbulent channels being one of the most fundamental test cases in anisotropic turbulence, a great deal of knowledge has been gained on the flow dynamics over a large range of regimes. Direct numerical simulations have enabled researchers to obtain detailed statistical characteristics such as flow spectra and two-point correlations.

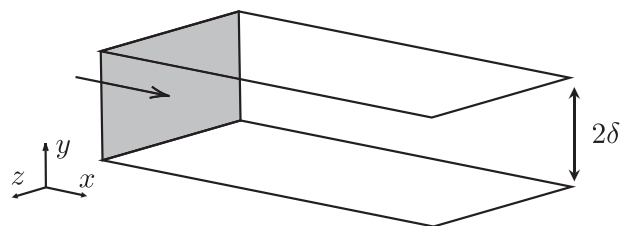


FIG. 1. Channel flow case and coordinate system.

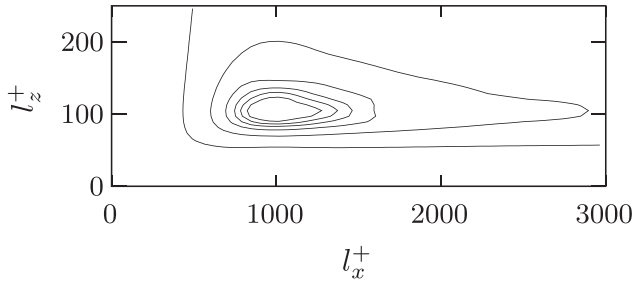


FIG. 2. Contour plot of the two-dimensional velocity spectrum imposed.

The averaged flow field is non-homogeneous in the wall-normal direction, symmetric with respect to the mid-channel and homogeneous in the streamwise and spanwise directions. Knowing that, the inflow data for a turbulent channel can be formally represented by

$$u'_i(x, y, z) = \sum_{k_x} \sum_{k_z} \sum_l \sqrt{C(k_x, k_z) \lambda(l)} q_i(k_x, k_z, l, y) \times e^{i(k_x x + k_z z)} \phi(j, k, l), \quad (5)$$

where k_x and k_z are the wavenumbers in the homogeneous directions, l is the wall-normal mode index, q is the wall-normal eigenmode, λ is the eigenvalue, C is the spectrum imposed, and ϕ is a random number.

The three-dimensional digital filters $f_{k_z, l}$ are obtained by taking the inverse transform in the streamwise direction of Eq. (5)

$$f_{k_z, l}(x, y, z) = \sum_{k_x} \sqrt{C(k_x, k_z) \lambda(l)} q_i(k_x, k_z, l, y) e^{i(k_x x + k_z z)}. \quad (6)$$

Finally, the three-dimensional signal, of which each spanwise-wall-normal slice will be used as an inflow realization, is obtained by convoluting the filters with a random signal

$$u'_i(x, y, z) = \sum_{k_z} \sum_l (f_{k_z, l} \otimes \phi)(x, y, z). \quad (7)$$

Subsections III A 1 and III A 2 explain the procedure followed to construct the filters for the channel case, highlighting the approximations made to obtain a shape estimation of the correlation tensor and the power spectrum.

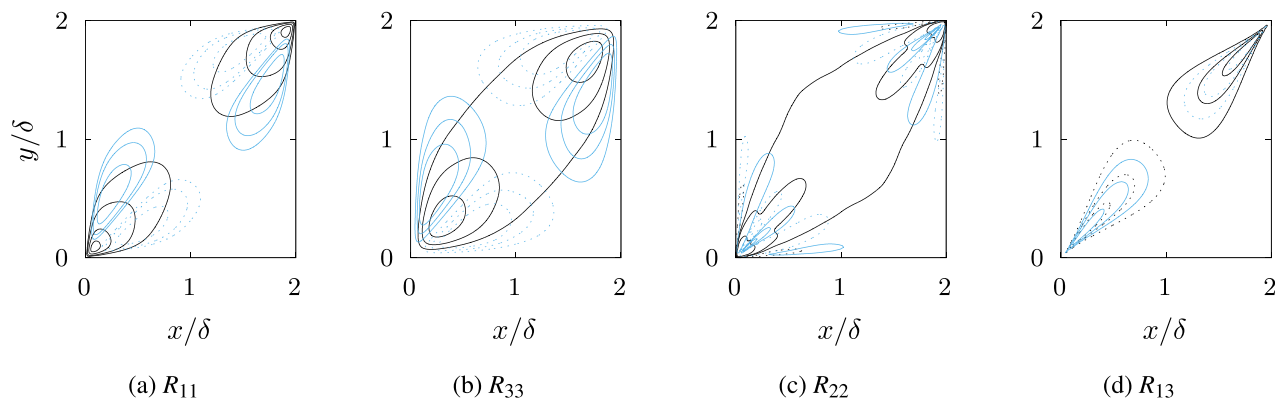


FIG. 3. Contour plots of the two-point velocity correlation tensor. Black contours represent the real part; blue contours represent the imaginary part; and dashed lines represent negative values.

1. Velocity spectrum in periodic directions

As explained in Sec. II A, an energy distribution is needed for each of the homogeneous directions. Turbulent flows contain a wide range of length scales, but most of the energy is often located within a limited scope. In isotropic turbulence, the well-known Kolmogorov spectrum with the energy proportional to a power law of the wavenumber can be used. For a channel case, multiple DNS analyses are available, see Andrade *et al.* (2018), Mizuno (2016), and Lee and Moser (2019). The main concentration of energy is located at wavenumber ratios $k_z/k_x \gtrsim 10$, corresponding to elongated structures present in the channel. Various wall-normal spectral regimes have been identified in Lee and Moser (2019) and Mizuno (2016), highlighting the wavelength variations of the channel streaks with the wall-normal direction. However, a reasonable assumption can be made by considering a uniform spectrum in the wall-normal direction. Figure 2 shows the spectrum with a maximum spanwise wavelength of $l_z^+ = 100$ and a ratio $l_x/l_z = 10$.

2. Wall-normal autocorrelation

The construction of the wall-normal covariance tensor as a function of the wavenumber is guided by previous research from Townsend (1976), Kim *et al.* (1987), and Nawab and di Mare (2018). Writing the one-dimensional correlation tensor $R_{ij}(y^{(1)}, y^{(2)}) = \langle u_i(y^{(2)}) u_j^*(y^{(1)}) \rangle$, the continuity equation for a periodic channel in wavenumber space is

$$\begin{cases} ik_x R_{1,1}(y^{(1)}, y^{(2)}, k_x, k_z) + ik_z R_{1,2}(y^{(1)}, y^{(2)}, k_x, k_z) \\ + \frac{\partial}{\partial y^{(2)}} R_{1,3}(y^{(1)}, y^{(2)}, k_x, k_z) = 0, \\ ik_x R_{2,1}(y^{(1)}, y^{(2)}, k_x, k_z) + ik_z R_{2,2}(y^{(1)}, y^{(2)}, k_x, k_z) \\ + \frac{\partial}{\partial y^{(2)}} R_{2,3}(y^{(1)}, y^{(2)}, k_x, k_z) = 0, \\ ik_x R_{3,1}(y^{(1)}, y^{(2)}, k_x, k_z) + ik_z R_{3,2}(y^{(1)}, y^{(2)}, k_x, k_z) \\ + \frac{\partial}{\partial y^{(2)}} R_{3,3}(y^{(1)}, y^{(2)}, k_x, k_z) = 0. \end{cases} \quad (8)$$

The continuity constraint combined with the symmetry condition of the two-point correlation leaves three components of the tensor to be specified. The three normal components could be chosen, but then a

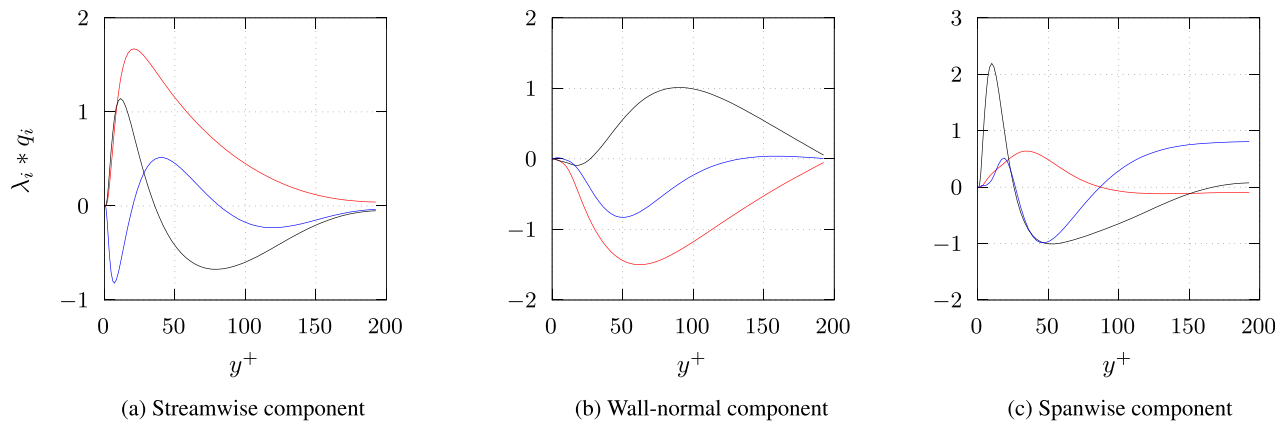


FIG. 4. Real part of the first three wall-normal eigenfunctions at peak spectrum. Red curve—first mode; black curve—second mode; and blue curve—third mode.

linear system of differential equations must be solved. The system is likely to have an infinite number of solutions and must be solved in a least squares fashion. Taking another approach, if two normal and one non-diagonal components are specified, the system can be solved immediately by substitution. The equations suggest that the approximations of the correlation must be complex. The imaginary part controls the phase of the velocity field, which is related to the structure and shape of the turbulent eddies, see Keating *et al.* (2004). Nawab and di Mare (2018) give an idea of the full shape of the correlation tensor.

The covariance tensor is built from the exponential expression given in Eq. (3) with the characteristic length scale chosen to be the harmonic average of the turbulent length scale and the wavelength of the mode considered. One assumption made is that the wall-normal variance profile does not change with the wavenumber considered, and only the extent in space of the correlation is changing. This is not the case as shown in Lee and Moser (2019), but there does not exist enough data on the subject to make a better representation. Figure 3 shows the contours of the velocity correlation tensor for spanwise wavelengths of $l_z^+ = 50$ and streamwise wavelengths of $l_x^+ = 500$, and the real and imaginary components follow correctly the trends present in the data from Nawab and di Mare (2018).

The first three one-dimensional eigenfunctions for different velocity components are plotted in Fig. 4. The modes represent the influence on the velocity fluctuations of the turbulent structures present in the flow. The eigenfunctions for the streamwise velocity have most of the energy near the wall, whereas for the other components, the overall peak energy is located further away from the wall. The streamwise and wall-normal components compare well with the results from Moin and Moser (1989). The modes for the spanwise components on the other side are imperfect, and this is because all the spanwise velocity correlation components are solved for through the divergence equation, and therefore, no variance data for the spanwise component have been used. The study of the eigenmodes showed the need for a complete expression of the correlation tensor—if components are missing, the remaining components become uncorrelated and the relative amplitude and phase between the modes are not correct.

The three-dimensional shape of the eigenfunctions is dictated by the homogeneous directions, and the modes will have an oriented

periodic eddy structure corresponding to their wavenumber, as detailed by Ball *et al.* (1991).

3. Simulation setup

Strictly speaking, the geometry of a channel flow is completely defined by the channel height, 2δ . However, the computational domain has to be of finite size, leading to the introduction of the streamwise and spanwise lengths, L_x and L_z . The flow is simulated between two viscous walls, and periodic boundaries are applied in spanwise directions. The Reynolds number Re_τ , based on the friction velocity and the channel half-width investigated, is 180 at a Mach number $Ma = 0.3$.

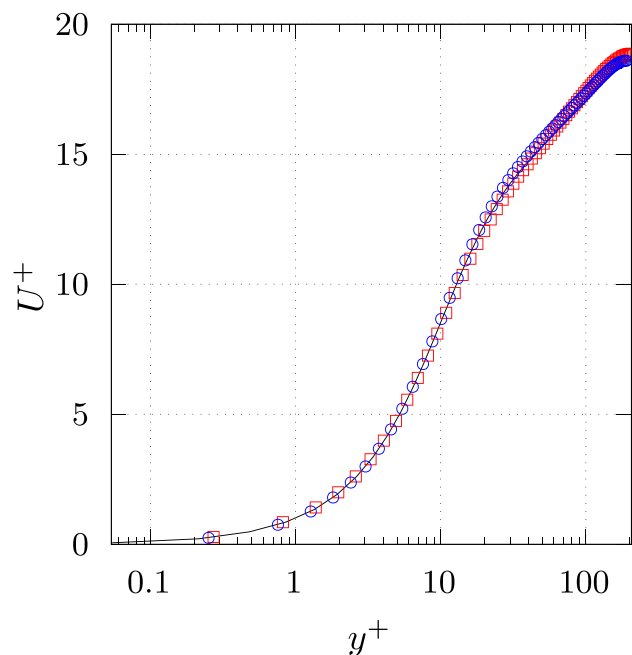


FIG. 5. Mean velocity profiles. Black curve—DNS data from Moser *et al.* (1999), blue circles—periodic channel, and red squares—channel with inflow at $x/\delta = 2$.

The computational domain size in the streamwise and spanwise directions is $(8\pi\delta, 4/3\pi\delta)$, found by Kim *et al.* (1987) to be enough for the flow variables to become uncorrelated at maximum streamwise and spanwise separation. The grid size is $(256 \times 144 \times 128)$ with a grid stretching in the wall-normal direction detailed in Pirozzoli and Orlandi (2021). To capture the physics, the first cell is in the viscous sub-layer, $\Delta y^+ \mathcal{O}(1)$, and having $\Delta x^+ \mathcal{O}(10)$ and $\Delta z^+ \mathcal{O}(5)$ is sufficient to resolve small-scale structures near the walls.

The simulation with the inflow generator will be compared against DNS data available from Kim *et al.* (1987) and against a

streamwise periodic channel run with the same setup as the channel with turbulent inflow. The mass flow of the periodic channel was kept constant with the addition of an artificial body force.

4. Mean quantities

Figure 5 plots the mean velocity profiles made dimensionless by the wall-shear velocity. The profile of the simulation with inflow correctly matches the well-known DNS results. This is expected as the profile imposed came from DNS calculations, but it shows that the mean quantities downstream of the inlet plane are not altered by the introduced fluctuations. The periodic channel case was initialized with a simple randomized parabolic profile. The correct prediction of the mean streamwise velocity profile shows the ability of the solver and the mesh to resolve appropriately the scales of interest.

5. Velocity fluctuations

To evaluate the development length, the velocity variances are compared with Kim *et al.* (1987) at different streamwise locations. Figure 6 shows the streamwise evolution of the Reynolds normal stresses. Overall, a very good fit is reached after $x/\delta \simeq 6$, less than 5% RMS error, but less than 10% RMS deviation is reached after $x/\delta \simeq 3$. While the guessed shape for the streamwise and spanwise component is close to the actual profile for the streamwise and wall-normal component, the fit and amplitude is less accurate for the spanwise component—as explained in Sec. III A 4. This is a result of the divergence condition that was applied. The streamwise profile at the inflow is overestimated toward the mid-channel but recovers slowly until $x/\delta \simeq 6$. The spanwise and wall-normal profiles have inaccurate near-wall behavior but reach a better agreement near the mid-channel.

Figure 7 plots the spanwise correlation at two different wall-normal positions, near the wall and near mid-channel. At the inflow, it can be seen that the realizations are correlated and the sinc shape is in accordance with the spectrum prescribed, with a negative peak at small separation. The decay for $x/\delta = 6$ follows the same trend as the correlations available in Kim *et al.* (1987) and Abe *et al.* (2001). At the inlet, the failure to capture the correct spanwise correlation away from the

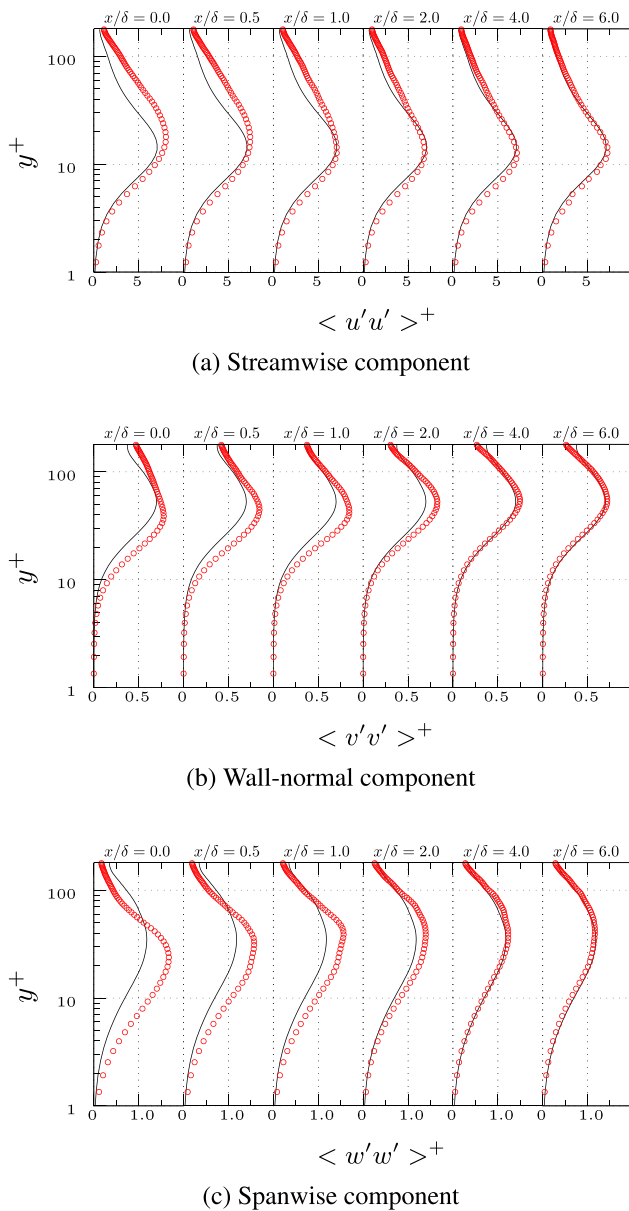


FIG. 6. Streamwise development of the dimensionless time-averaged velocity variances.

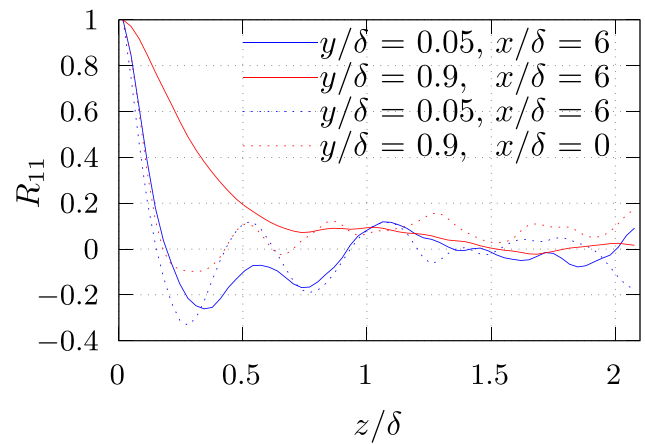


FIG. 7. Spanwise two-point correlation at selected streamwise and spanwise locations.

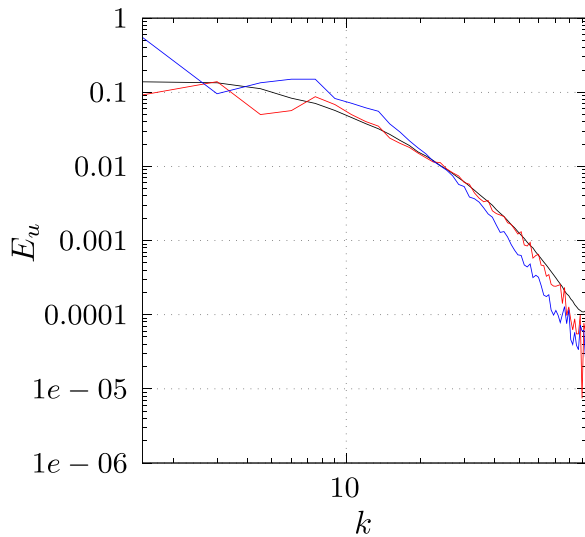


FIG. 8. Normalized spanwise spectrum of the streamwise velocity component at mid-channel averaged over $x/\delta = [0.6-0.7]$. Black curve—DNS data from Moser *et al.* (1999); red curve—reference inflow run, energy cutoff = 0.95; and blue curve—energy cutoff = 0.6.

wall comes from the assumption that the streamwise–spanwise spectrum is constant in the wall-normal direction.

6. Inflow parameters and performance

The inflow technique relies on a number of turbulent parameters that must be carefully chosen in order to obtain accurate inflow realization.

First, the streamwise extent of the inflow domain should be greater than the integral timescale of the flow field, which is necessary to ensure the field becomes uncorrelated.

In the exponential expression chosen to estimate the wall-normal correlation, the extent of the wall-normal correlation is dictated by the magnitude of the decay constant. If the decay is excessively swift, the

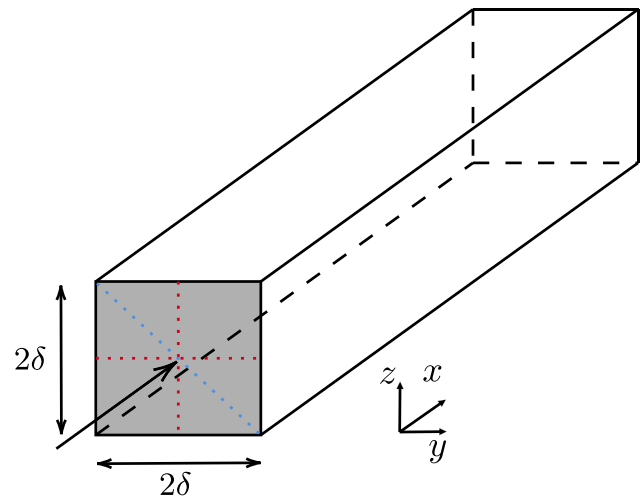


FIG. 9. Square duct diagram and coordinate system.

covariance matrix becomes virtually diagonal and the fluctuations uncorrelated. On the contrary, the variables become too correlated at large separations and the inflow realizations will resemble a set of bands in the wall-normal direction. The top and bottom sides of the channel will become too correlated, which is not physical.

Eigenanalysis allows for a direct sorting of the modes based on energy. The energy cutoff should be proportional to the scales resolvable by the mesh of the main simulation. It is desirable to retain as much energy as possible, but it adds a memory and computational overhead to store and reconstruct all the length scales. The spectral content of the generated fields is important for the Reynolds stress budget equation. As explained in Keating *et al.* (2004), the production rate term is a function of the mean flow field and the Reynolds stress; hence, from Fig. 6, it can be assumed that the magnitude is sensible even close to the inflow plane. However, to correctly model the dissipation term, the spectral content in the flow field must follow the distribution of a real turbulent flow along the wall-normal direction. If only large scales are present in the flow, the kinetic energy dissipation

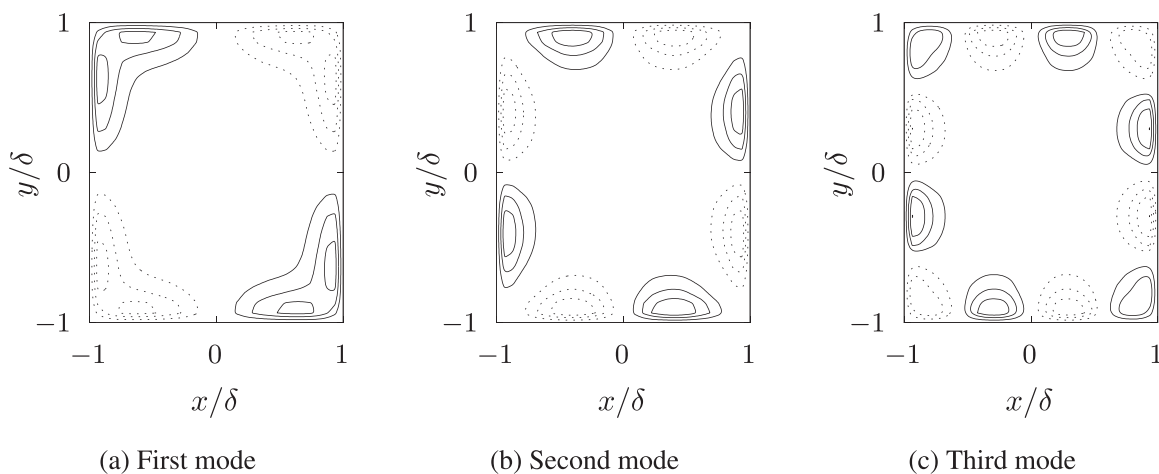


FIG. 10. Contour plots of streamwise component of the first three modes. Dashed lines represent negative values.

will be largely underestimated. The correct distribution will be reached further downstream once the large structures have broken down and the balance between production and dissipation is restored. Figure 8 illustrates this by comparing the spanwise spectrum downstream of the inflow for different energy cutoffs, one where nearly all the length scales are represented and a second case where only the dominant scales are kept. The case with lower energy cutoff does not have the correct decay unlike the case with higher energy threshold. The performance of the inflow generator depends on several factors, including the size of the filter, the number of grid points at the inlet, and the number of modes retained. To prioritize runtime performance or ensure repeatability, the inflow fields can be generated prior the simulation and simply read at runtime. In terms of resources, the entire inflow generation process uses 4%–8% of the total simulation time, depending on the energy cutoff chosen. While the proposed method requires additional resources compared to the original filter method by Klein *et al.* (2003), it remains significantly lighter than precursor simulations and hybrid volumetric forcing simulations. The performance of the algorithm can be further enhanced by applying techniques outlined in Kempf *et al.* (2012), for example.

B. Square duct flow

The second test case studied is a straight duct with a square cross section at a Reynolds number based on the friction velocity of 220 and a bulk Mach number of 0.2. There has been a strong interest in rectangular duct flows mainly because of the cross-sectional motions (Fig. 9). The time-averaged flow has four statistically symmetric quadrants, each containing a pair of counter rotating vortices. These turbulence-born secondary flows, named of Prandtl's second kind, will test the ability of the inflow method to generate coherent structures capable of reproducing the gradients in the Reynolds stresses to produce the vorticity necessary to drive the secondary flows, Brundrett and Baines (1964). Multiple DNS studies on duct flows are available, see, for example, Gavrilakis (1992) or Pirozzoli *et al.* (2018).

1. Streamwise turbulent kinetic energy spectra

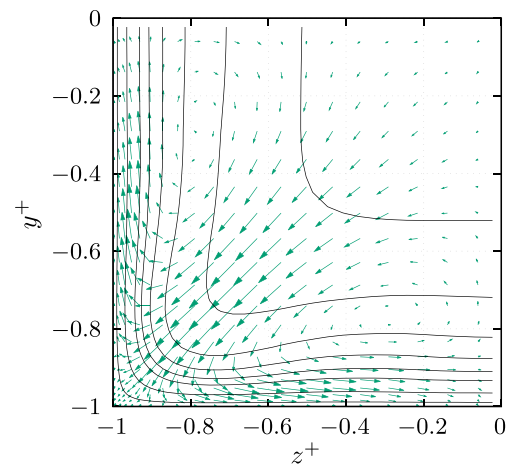
Square ducts have only one homogeneous direction, and the streamwise kinetic energy spectra can be approximated by simple Kolmogorov spectra, agreeing with results from Khan *et al.* (2020) and Huser and Biringen (1993).

2. Spanwise and wall-normal correlation

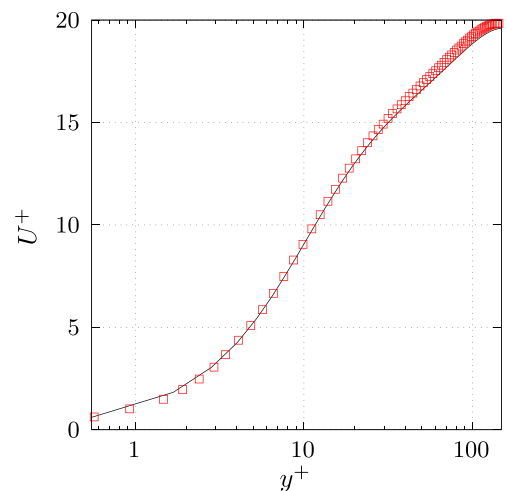
The correlation tensor is constructed using the expression in Eq. (3). Similarly to Sec. III A 2, only three components of the tensor are guessed and the remaining are set through the divergence-free condition and the symmetries of the problem. The symmetries of the problem imply that each eigenmode comes in quartet. The streamwise component of the first three families of modes is plotted in Fig. 10.

3. Mean quantities

The contours of mean velocity are plotted in Fig. 11(a), and the secondary flows are highlighted using velocity vectors. While the magnitude of the secondary flows is not of the same order of that of the mean axial flow, they are responsible for the swelling of mean axial



(a) Vector plot of the cross-section mean velocity and contours of the streamwise component



(b) Mean dimensionless streamwise velocity profiles. Black curve - data from Pirozzoli *et al.* (2018), red squares - square duct with inflow

FIG. 11. Mean quantities for the square duct case.

velocity contours toward the corners, as observed by Brundrett and Baines (1964). The mean velocity profile on the wall bisector is plotted on Fig. 11(b) and matches well the data from Pirozzoli *et al.* (2018).

C. Fluctuating quantities

Figure 12 plots the development of the time-averaged velocity variances. It is observed again that, while not perfect, a close agreement is reached after a length of 6δ , RMS error of 6%. The spanwise component, which was obtained mainly through the divergence-free condition, is largely overpredicted at the inflow but quickly settles downstream.

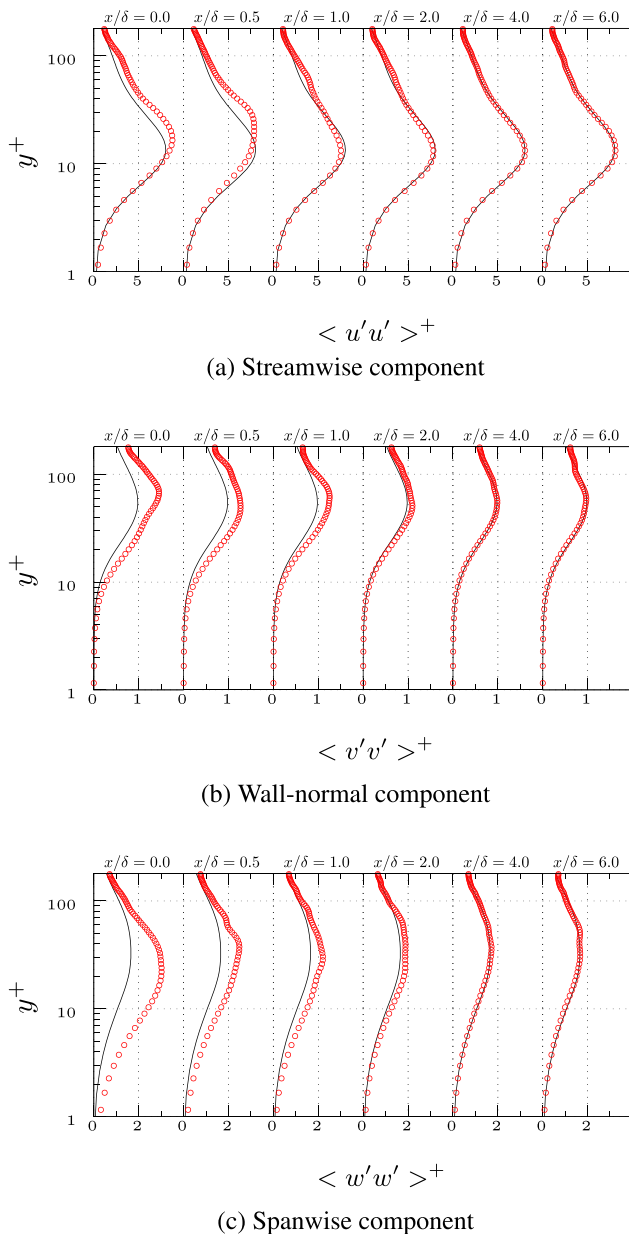


FIG. 12. Development of dimensionless time-averaged velocity variances.

IV. CONCLUSION

The current work presented an extension to a filter-based method for generating statistically realistic divergence-free turbulent data. The procedure is built around the factorization of the covariance tensor and the conservation of mass. In the non-homogeneous directions, an approximation of the complex correlation tensor is constructed from variance data combined with an exponential decay. The incompressible continuity equation was enforced to lower the number of components to be guessed and to ensure the generated field is

divergence-free. The periodic directions are assembled with trigonometric functions based on an appropriate energy distribution.

The method was tested on two wall-bounded turbulence cases and showed good agreement with existing data. The eigenmodes for both cases capture the regions of high variance. The inflow generator was able to generate realistic fluctuations for the reproduction of the second moments within a short distance of the inlet plane while keeping a constant first moment. The reconstructed second moments at the inflow plane have a realistic shape and adjust quickly to the targeted profile. Only the components solved with the continuity equation gave less accurate approximations in the variance of the realizations. The assumption of constant properties in the wall-normal direction leads to acceptable results while being the source of most inaccuracies—further developments should take the different wall regimes into account. Component-wise spectra could also be introduced.

The main interest of the proposed method is the ability to generate realistic data for scale-resolving simulations with a short development length from readily available statistics. The approach has a small computational cost overhead compared to other inflow techniques and is highly versatile. The performance has been proven and potential further development highlighted.

ACKNOWLEDGMENTS

The authors are grateful for the support from Rolls-Royce PLC and the EPSRC Center for Doctoral Training in Future Propulsion and Power. The authors would also like to acknowledge the use of the University of Oxford Advanced Research Computing (ARC, Richards, 2015), facility in carrying out this work.

AUTHOR DECLARATIONS

Conflict of Interest

The authors have no conflicts to disclose.

Author Contributions

Yann Drèze: Investigation (lead); Methodology (equal); Software (lead); Validation (lead); Writing – original draft (lead); Writing – review & editing (lead). **Muting Hao:** Methodology (lead); Software (supporting); Supervision (supporting); Writing – review & editing (supporting). **Luca di Mare:** Investigation (supporting); Methodology (equal); Resources (lead); Supervision (lead); Writing – review & editing (lead).

DATA AVAILABILITY

The data that support the findings of this study are available from the corresponding author upon reasonable request.

REFERENCES

- Abe, H., Kawamura, H., and Matsuo, Y., “Direct numerical simulation of a fully developed turbulent channel flow with respect to the Reynolds number dependence,” *J. Fluids Eng.* **123**(2), 382–393 (2001).
- Andrade, J. R., Martins, R. S., Mompean, G., Thais, L., and Gatski, T. B., “Analyzing the spectral energy cascade in turbulent channel flow,” *Phys. Fluids* **30**(6), 065110 (2018).
- Bakewell, H. P. and Lumley, J. L., “Viscous sublayer and adjacent wall region in turbulent pipe flow,” *Phys. Fluids* **10**(9), 1880–1889 (1967).

- Ball, K. S., Sirovich, L., and Keefe, L. R., "Dynamical eigenfunction decomposition of turbulent channel flow," *Int. J. Numer. Methods Fluids* **12**, 585–604 (1991).
- Brundrett, E. and Baines, W. D., "The production and diffusion of vorticity in duct flow," *J. Fluid Mech.* **19**(3), 375–394 (1964).
- Dhamankar, N. S., Martha, C. S., Situ, Y., Aikens, K. M., Blaisdell, G. A., Lyrntzis, A. S., and Li, Z., "Digital filter-based turbulent inflow generation for jet aeroacoustics on non-uniform structured grids," AIAA Paper No. 2014-1401, 2014.
- Dhamankar, N. S., Blaisdell, G. A., and Lyrntzis, A. S., "Overview of turbulent inflow boundary conditions for large-eddy simulations," *AIAA J.* **56**(4), 1317–1334 (2018).
- di Mare, L. and Jones, W., "Algebraic and operator methods for generation of inflow data for LES and DNS," in *Fourth International Symposium on Turbulence and Shear Flow Phenomena* (Begell House Inc., 2005).
- di Mare, L., Klein, M., Jones, W. P., and Janicka, J., "Synthetic turbulence inflow conditions for large-eddy simulation," *Phys. Fluids* **18**(2), 025107 (2006).
- Fukami, K., Nabae, Y., Kawai, K., and Fukagata, K., "Synthetic turbulent inflow generator using machine learning," *Phys. Rev. Fluids* **4**, 064603 (2019).
- Gavrilakis, S., "Numerical simulation of low-Reynolds-number turbulent flow through a straight square duct," *J. Fluid Mech.* **244**, 101–129 (1992).
- Hao, M., Hope-Collins, J., and di Mare, L., "Generation of turbulent inflow data from realistic approximations of the covariance tensor," *Phys. Fluids* **34**, 115140 (2022).
- Hoepffner, J., Naka, Y., and Fukagata, K., "Realizing turbulent statistics," *J. Fluid Mech.* **676**, 54–80 (2011).
- Hope-Collins, J. and di Mare, L., "Artificial diffusion for convective and acoustic low Mach number flows. I. Analysis of the modified equations, and application to Roe-type schemes," *J. Comput. Phys.* **475**, 111858 (2023).
- Huser, A. and Biringen, S., "Direct numerical simulation of turbulent flow in a square duct," *J. Fluid Mech.* **257**, 65–95 (1993).
- Keating, A., Piomelli, U., Balaras, E., and Kaltenbach, H.-J., "A priori and a posteriori tests of inflow conditions for large-eddy simulation," *Phys. Fluids* **16**(12), 4696–4712 (2004).
- Kempf, A., Wysocki, S., and Pettit, M., "An efficient, parallel low-storage implementation of Klein's turbulence generator for LES and DNS," *Comput. Fluids* **60**, 58–60 (2012).
- Ketterl, S. and Klein, M., "A band-width filtered forcing based generation of turbulent inflow data for direct numerical or large eddy simulations and its application to primary breakup of liquid jets," *Flow, Turbul. Combust.* **101**, 413 (2018).
- Khan, H., Anwar, S., Hasan, N., and Sanghi, S., "The organized motion of characterized turbulent flow at low Reynolds number in a straight square duct," *SN Appl. Sci.* **2**, 763 (2020).
- Kim, J. and Lee, C., "Deep unsupervised learning of turbulence for inflow generation at various Reynolds numbers," *J. Comput. Phys.* **406**, 109216 (2020).
- Kim, J., Moin, P., and Moser, R., "Turbulence statistics in fully developed channel flow at low Reynolds number," *J. Fluid Mech.* **177**, 133–166 (1987).
- Klein, M., Sadiki, A., and Janicka, J., "A digital filter based generation of inflow data for spatially developing direct numerical or large eddy simulations," *J. Comput. Phys.* **186**(2), 652–665 (2003).
- Kondo, K., Murakami, S., and Mochida, A., "Generation of velocity fluctuations for inflow boundary condition of LES," *J. Wind Eng. Ind. Aerodyn.* **67–68**, 51–64 (1997).
- Le, H., Moin, P., and Kim, J., "Direct numerical simulation of turbulent flow over a backward-facing step," *J. Fluid Mech.* **330**, 349–374 (1997).
- Lee, M. and Moser, R. D., "Spectral analysis of the budget equation in turbulent channel flows at high Reynolds number," *J. Fluid Mech.* **860**, 886–938 (2019).
- Lumley, J. L., "Coherent structures in turbulence," in *Transition and Turbulence* (Academic Press, 1981), pp. 215–242.
- Lund, T. S., Wu, X., and Squires, K. D., "Generation of turbulent inflow data for spatially developing boundary layer simulations," *J. Comput. Phys.* **140**(2), 233–258 (1998).
- Meux, B., Audebert, B., Manceau, R., and Perrin, R., "Anisotropic linear forcing for synthetic turbulence generation in LES and hybrid RANS/LES modeling," *Phys. Fluids* **27**, 035115 (2015).
- Mizuno, Y., "Spectra of energy transport in turbulent channel flows for moderate Reynolds numbers," *J. Fluid Mech.* **805**, 171–187 (2016).
- Moin, P. and Moser, R. D., "Characteristic-eddy decomposition of turbulence in a channel," *J. Fluid Mech.* **200**, 471–509 (1989).
- Moser, R. D., Kim, J., and Mansour, N. N., "Direct numerical simulation of turbulent channel flow up to $Re_\tau = 590$," *Phys. Fluids* **11**(4), 943–945 (1999).
- Nawab, A. and di Mare, L., "Re scaling of pod modes in plane channel flow," *Phys. Fluids* **30**(5), 055109 (2018).
- Pirozzoli, S., Modesti, D., Orlandi, P., and Grasso, F., "Turbulence and secondary motions in square duct flow," *J. Fluid Mech.* **840**, 631–655 (2018).
- Pirozzoli, S. and Orlandi, P., "Natural grid stretching for DNS of wall-bounded flows," *J. Comput. Phys.* **439**, 110408 (2021).
- Rai, M. M. and Moin, P., "Direct numerical simulation of transition and turbulence in a spatially evolving boundary layer," *J. Comput. Phys.* **109**(2), 169–192 (1993).
- Richards, A. (2015). "University of Oxford advanced research computing," Zenodo. [10.5281/zenodo.22558](https://doi.org/10.5281/zenodo.22558)
- Spille-Kofoff, A. and Kaltenbach, H.-J., "Generation of turbulent inflow data with a prescribed shear-stress profile," Report No. ADP013648 (2001).
- Townsend, A. A., *The Structure of Turbulent Shear Flow*, 2nd ed. (Cambridge University Press, 1976).
- Treleaven, N., Staufer, M., Spencer, A., Garmory, A., and Page, G., "Application of the PODFS method to inlet turbulence generated using the digital filter technique," *J. Comput. Phys.* **415**, 109541 (2020).
- Wu, X., "Inflow turbulence generation methods," *Annu. Rev. Fluid Mech.* **49**(1), 23–49 (2017).
- Yousif, M. Z. G., Zhang, M.-T., Yu, L., Vinuesa, R., and Lim, H., "A transformer-based synthetic-inflow generator for spatially developing turbulent boundary layers," *arXiv:2206.01618* (2022).